COMMUNICATIONS IN COMPUTATIONAL PHYSICS
Vol. **5**, No. 1, pp. 61-83

Commun. Comput. Phys.
January 2009

Numerical Simulations of Fiber Sedimentation in Navier-Stokes Flows

Jin Wang[1,*] and Anita Layton[2]

[1] *Department of Mathematics and Statistics, Old Dominion University, Norfolk, VA 23529, USA.*
[2] *Department of Mathematics, Box 90320, Duke University, Durham, NC 27708, USA.*

Received 11 February 2008; Accepted (in revised version) 13 April 2008

Available online 15 July 2008

Abstract. We perform numerical simulations of the sedimentation of rigid fibers suspended in a viscous incompressible fluid at nonzero Reynolds numbers. The fiber sedimentation system is modeled as a two-dimensional immersed boundary problem, which naturally accommodates the fluid-particle interactions and which allows the simulation of a large number of suspending fibers. We study the dynamics of sedimenting fibers under a variety of conditions, including differing fiber densities, Reynolds numbers, domain boundary conditions, etc. Simulation results are compared to experimental measurements and numerical results obtained in previous studies.

AMS subject classifications: 76D05, 76M25

Key words: Fiber sedimentation, immersed boundaries, Navier-Stokes equations.

1 Introduction

The sedimentation of solid particles can be found in many natural phenomena and industrial applications, e.g., the flow of pollutants in rivers and in the atmosphere, the clarification of liquids, and the separation of particles of differing masses. Nonetheless, despite the wide applicability of particle sedimentation, some of its fundamental properties remain to be understood. One of the challenges in understanding these properties lies in the long-range hydrodynamic interactions among the particles.

Much effort has been directed to studying the sedimentation process of spherical particles. For instance, the mean sedimentation velocity and the velocity fluctuations of the particles have been investigated experimentally [27] and theoretically [3, 11] (and see references therein). In contrast, the sedimentation of non-spherical particles is less well-understood. Owing to the anisotropic nature of the particles, the suspension structure

*Corresponding author. *Email addresses:* j3wang@odu.edu (J. Wang), alayton@math.duke.edu (A. Layton)

and fiber orientation have a significant impact on the sedimentation velocity. Also, unlike spheres, isolated fibers may have motion in the direction perpendicular to gravity.

Previous fiber experiments have measured the settling speed and orientation of sedimenting marked fibers. Experiments by Herzhaft et al. [17] revealed a dilute regime of inhomogeneous sedimentation in which the fibers tend to align in the direction of gravity and to clump together in packets. Experiments by Turney et al. [33] and by Anselmet [1] suggests that, in the semi-dilute regime, fiber settling is hindered at sufficiently high volume fractions.

Although not as extensively investigated as spherical particles, there have been several numerical studies on fiber suspensions. Butler and Shaqfeh [9] and Fan et al. [13] presented numerical simulation to fiber suspensions and compared their results to experimental data. Tornberg and co-workers developed a numerical method, based on a non-local slender body approximation that yields a system of coupled integral equations, to simulate rigid and flexible fiber suspensions at zero Reynolds number regime [31,32]. Their simulation results show settling and clustering behaviors consistent with experimental measurements previously reported. In addition, Kuusela et al. [20] performed numerical calculations of the dynamics of sedimenting prolate spheroids at a low Reynolds number 0.3.

A goal of this work is to study the behaviors of sedimenting fibers under differing conditions, including differing Reynolds number flows, fiber densities, boundary conditions, etc. To achieve that goal, we formulated a mathematical model of sedimenting thin, rigid fibers as a two-dimensional (2D) immersed boundary problem. The immersed boundary approach was first developed by Peskin [26] for solving the full incompressible Navier-Stokes equations with moving boundaries. The immersed boundary method was originally developed for studying blood flow through a beating heart [25], but has since been applied to a wide variety of problems, including inner ear fluid dynamics [5], bacterial swimming [12], sperm motility in the presence of boundaries [14], cilliary beating [7], flow through an arteriole [2], etc. In particular, Stockie [28] applied this method to simulate the motion of a single pulp fiber in a linear shear flow. The immersed boundary approach offers much flexibility: the Reynolds number can be set to be any arbitrary value, the immersed boundaries as well as the fluid domain can theoretically be of arbitrary shape, and there is little constraint on the domain boundary conditions. In the current problem, the fibers are modeled as immersed boundaries that exert forces on the surrounding fluid when subjected to gravity.

Using the immersed fiber model, we study, in terms of sedimentation velocity and fiber distribution, the effects of fiber density, initial fiber distribution, Reynolds number, and domain boundary conditions. In general, our simulation results are consistent with experimental observations reported in literature.

The paper is organized as follows. In Section 2, an immersed boundary model is introduced. In Section 3, numerical simulations are performed using the method described in Section 2 for fibre suspensions in a fluid with a nonzero Reynolds number. Some discussions are presented in the final section.

2 An immersed boundary model

In this section, we formulate a computational hydrodynamic model to simulate the suspensions of rigid thin fibers in a viscous incompressible fluid. The model is based on the immersed boundary formulation [26]. In an immersed boundary problem, the fluid is computed on an Eulerian grid, whereas the immersed boundaries (i.e., the fibers in the current case) are tracked using Lagrangian coordinates. The fluid and boundaries interact as the boundaries exert forces on the fluid, and as the fluid pushes the boundaries. To reduce the computational efforts, the current fiber model is formulated in two spatial dimensions (2D); nonetheless, the extension to three dimensions (3D) is straightforward. The fibers are assumed to be infinitely thin and are represented by one-dimensional curves.

Let us denote the spatial coordinates by (x,y), the temporal coordinate by t, the velocity by $\mathbf{u}$, and the pressure by p. We assume that the density of the fiber ρ_{fiber} is slightly greater than the density of the fluid ρ_{fluid}, i.e.,

$$\Delta\rho \equiv \rho_{\text{fiber}} - \rho_{\text{fluid}} \ll \rho_{\text{fluid}}.$$

With this assumption, we make the Boussinesq approximation and assume that the average density of the fiber-fluid suspension can be approximated by that of the fluid. After non-dimensionalization, the following incompressible Navier-Stokes equations are used to describe the fluid motion,

$$\mathbf{u}_t + (\mathbf{u}\cdot\nabla)\mathbf{u} = -\nabla p + \frac{1}{Re}\nabla^2\mathbf{u} + \sum_m \mathbf{F}_m, \tag{2.1}$$

$$\nabla\cdot\mathbf{u} = 0, \tag{2.2}$$

where Re is the Reynolds number. The subscript m indices the fibers, $1\le m\le M$, where M denotes the total number of fibers. The force term $\mathbf{F}_m$ arises from the gravitational force acting on the mth fiber and from the elastic forces generated in the course of fluid-fiber interaction.

The forces $\mathbf{F}_m$ in Eq. (2.1) are localized to the neighborhood of the immersed fibers; the x- and y-components are given by

$$F_{m,i}(\mathbf{x},t) = \int_0^{L_0} f_{m,i}(s,t)\delta(\mathbf{x}-\mathbf{X}_m(s,t))ds, \tag{2.3}$$

where $i=1,2$ denote the x- and y-components; L_0 is the length of a fiber at its relaxed state; $\mathbf{X}_m(s,t)$ gives the location of the mth fiber at time t, parameterized by the length s at the relaxed state for $0\le s\le L_0$; $f_{m,i}(s,t)$ is the force strength at this point; and δ is the two-dimensional delta function. The force strength $\mathbf{f}_m$ is given by the sum of the gravitation force $\mathbf{f}_g$, a pseudo anti-bending force $\mathbf{f}_b$, and a tension force $\mathbf{f}_T$:

$$\mathbf{f}_m(s,t) = \mathbf{f}_g + \mathbf{f}_b + \mathbf{f}_T. \tag{2.4}$$

In our model, the fibers sediment due to their higher density compared to the fluid. We assume that the density difference, $\Delta\rho$, is small and the gravitational force only acts on fibers (a delta distribution):

$$\mathbf{f}_g = \Delta\rho\mathbf{g}, \tag{2.5}$$

where $\mathbf{g}$ is the gravitational acceleration. The same approach was used by Hopkins and Fauci [19].

The tension force is given by

$$\mathbf{f}_T = \frac{\partial}{\partial s}\left(T_m(s,t)\boldsymbol{\tau}(s,t)\right), \tag{2.6}$$

where the line tension $T_m(s,t)$ is

$$T_m(s,t) = T_0\left(\left|\frac{\partial \mathbf{X}_m(s,t)}{\partial s}\right| - 1\right). \tag{2.7}$$

The tension coefficient T_0 describes the elastic properties of the fiber and is assumed to be a constant in this model. Because we aim to model rigid fibers in this study, the coefficient T_0 is set to a large value ($T_0 = 1000$) to maintain the shape of the fibers. Mathematically, the tension $T_m(s,t)$ acts as a Lagrangian multiplier to ensure that the fibers remain inextensible. The vector tangential to the fiber is given by $\boldsymbol{\tau}(s,t)$, where

$$\boldsymbol{\tau}(s,t) = \frac{\partial \mathbf{X}_m/\partial s}{|\partial \mathbf{X}_m/\partial s|}. \tag{2.8}$$

Thus, the force density can be computed directly from the location $\mathbf{X}_m$ of the fiber. Note that at the relaxed state, $\partial \mathbf{X}_m/\partial s = 1$ and the tension vanishes.

The pseudo anti-bending force $\mathbf{f}_b$ represents the forces that the fibers exert on the fluid to maintain their rigidity. The positions of the rigid fibers are computed by allowing the two ends of the fibers to move at the velocity of the local fluid, i.e.,

$$\frac{\mathrm{d}\mathbf{X}_m(s,t)}{dt} = \mathbf{u}(\mathbf{X}_m(s,t),t), \tag{2.9}$$

where $s = 0$ and L_0. At time t, the mth fiber is represented by the straight line segment that passes through $\mathbf{X}_m(0,t)$ and $\mathbf{X}_m(L_0,t)$.

To approximate the pseudo anti-bending force, we use "fictitious markers", denoted by $\tilde{\mathbf{X}}_m$, to track the positions of the fibers if they were flexible and were allowed to move at the velocity of the local fluid, i.e.,

$$\frac{\mathrm{d}\tilde{\mathbf{X}}_m(s,t)}{dt} = \mathbf{u}(\tilde{\mathbf{X}}_m(s,t),t), \tag{2.10}$$

where $0 \le s \le L_0$. Thus, the two sets of markers agree at the two endpoints, i.e.,

$$\mathbf{X}_m(0,t) = \tilde{\mathbf{X}}_m(0,t), \quad \mathbf{X}_m(L_0,t) = \tilde{\mathbf{X}}_m(L_0,t).$$

The pseudo anti-bending force is given by a restoring force, based on Hooke's law, that arises from the discrepancy that evolves between two sets of markers over a time step Δt. Specifically, at time t, we set

$$\tilde{\mathbf{X}}_m(s,t)=\mathbf{X}_m(s,t) \quad \text{for } 0\le s\le L_0.$$

Then after Δt, the two sets of markers no longer agree except at the endpoints, and the pseudo anti-bending force is given by

$$\mathbf{f}_{b,m}(s,t+\Delta t)=k\left(\mathbf{X}_m(s,t+\Delta t)-\tilde{\mathbf{X}}_m(s,t+\Delta t)\right). \tag{2.11}$$

To approximate rigid fibers, we set the spring constant k to a large value ($k=1000$). Compared to the anti-bending force used in [32], which is given by the fourth-order arclength-derivative of the fiber profile, and to the feedback control force used in [6,15,21], our approach may be less physical (nonetheless, our simulation results are in reasonable agreement with experimental measurements), but it is also more stable and thus more suitable for long-time simulations.

Once all the above forces are generated, the motion of the fluid can be computed, and the two endpoint markers are advanced to the next time, t_{n+1}, using the no-slip condition (2.9). A line segment connecting these two endpoint markers gives the new position of the fiber. The fictitious markers are re-distributed equally along the fiber to start next cycle of computation.

In addition, our fluid solver, i.e., the numerical discretization of the Navier-Stokes equations, is based on the widely used projection formulation [4,8,10] which generally involves two steps. To advance the solution from t_n to t_{n+1}, we first calculate an intermediate velocity $\mathbf{u}^*$,

$$\frac{\mathbf{u}^*-\mathbf{u}^n}{\Delta t}+(\mathbf{u}^n\cdot\nabla)\mathbf{u}^n=-\nabla p^n+\frac{1}{2Re}\left(\nabla^2\mathbf{u}^*+\nabla^2\mathbf{u}^n\right)+\sum_m \mathbf{F}_m^n. \tag{2.12}$$

Then to impose incompressibility, the intermediate velocity $\mathbf{u}^*$ is projected onto the space of divergence-free fields to yield the new velocity at the time level $n+1$,

$$\nabla^2\phi=\frac{1}{\Delta t}\nabla\cdot\mathbf{u}^*, \tag{2.13}$$

$$\mathbf{u}^{n+1}=\mathbf{u}^*-\Delta t\nabla\phi, \tag{2.14}$$

$$\nabla p^{n+1}=\nabla p^n+\nabla\phi, \tag{2.15}$$

where an auxiliary function, ϕ, is introduced to count for the pressure increment.

We can now summarize our numerical procedure as follows. Let $\mathbf{X}_{m,q}$ represent the position of the qth marker in the mth fiber, where $q=1,2,\cdots,Q$; let also $\mathbf{u}_{i,j}^n$ denote the velocity at the grid point (x_i,y_j) at time t_n; and let $\mathbf{U}_{m,q}^n$ denote the velocity at the qth marker of the mth fiber at time t_n. At each time step, given $\mathbf{X}_{m,q}^n$, $\mathbf{u}_{i,j}^n$ and $\mathbf{U}_{m,q}^n$, we advance the solution to the next time step $n+1$ by the following procedure:

1. Compute the forces $\mathbf{F}^n_{m,i,j}$ at each grid node so that the Navier-Stokes equations can be solved on the grid. This requires spreading the boundary forces to the grid:

$$\mathbf{F}^n_{m,i,j} = \sum_q \mathbf{f}^n_{m,q} \mathbf{D}_h \left(\mathbf{x}_{ij} - \mathbf{X}^n_{m,q} \right) \Delta l. \tag{2.16}$$

The approximate delta function, denoted $\mathbf{D}_h$, is the product of two one-dimensional discrete delta functions,

$$\mathbf{D}_h(x,y) = \delta_h(x)\delta_h(y),$$

where h is the grid spacing. A common choice of δ_h is given by [10] [26]

$$\delta_h(x) = \begin{cases} \frac{1}{4h}\left[1+\cos\left(\frac{\pi x}{2h}\right)\right], & |x| \le 2h, \\ 0, & |x| > 2h. \end{cases} \tag{2.17}$$

2. Update the velocity field $\mathbf{u}^{n+1}_{i,j}$ by the projection method (2.12)-(2.15), using the calculated forces $\mathbf{F}^n_m$. For periodic spatial dimension(s), the Fast Fourier Transform (FFT) is performed. For spatial dimension(s) with non-periodic boundary conditions, central finite differences are used to discretize the spatial derivatives.

3. Interpolate the new velocity from the grid into the boundary points, and move the two endpoint markers in each fiber to their new positions using the kinematic condition:

$$\mathbf{U}^{n+1}_{m,q} = \sum_{i,j} \mathbf{u}^{n+1}_{ij} \mathbf{D}_h \left(\mathbf{x}_{i,j} - \mathbf{X}^n_{m,q} \right) h^2, \quad q = 1, Q; \tag{2.18}$$

$$\mathbf{X}^{n+1}_{m,q} = \mathbf{X}^n_{m,q} + \Delta t \mathbf{U}^{n+1}_{m,q}, \quad q = 1, Q. \tag{2.19}$$

The fictitious markers are then re-distributed equally along each fiber:

$$\tilde{\mathbf{X}}^{n+1}_{m,q} = \mathbf{X}^{n+1}_{m,1} + \frac{q-1}{Q-1}\left(\mathbf{X}^{n+1}_{m,Q} - \mathbf{X}^{n+1}_{m,1} \right), \quad q = 1,2,\cdots,Q. \tag{2.20}$$

Once the velocity field and interface profiles are updated, the above procedure is repeated for the next cycle of computation. This algorithm is found to be sufficiently robust and efficient to handle a large number of suspending fibers, and to allow for long-time simulations.

3 Numerical results

Numerical simulations are performed using the method described in the previous section for fiber suspensions in a fluid with a nonzero Reynolds number. A rectangular domain in the xy-plane is considered; periodicity is assumed in the vertical direction and, con-

sequently, the Fast Fourier Transform can be applied in y. With the vertical periodicity assumption, fibers which reach the bottom boundary will reenter at the top and interact with other fibers again. The horizontal boundary conditions are specified below. Gravity is assumed to act in the negative y-direction so that fibers are sedimenting downwards. The fluid is at rest initially, i.e., no base flow is added.

3.1 Fiber distribution

We first study the effects of fiber density on sedimentation behaviors. We consider a rectangular box of the size $[0,1]\times[0,10]$. We assume homogeneous Dirichlet boundary conditions in the x-direction, i.e., solid walls are assumed at $x=0$ and $x=1$. We first consider a small Reynolds number, $Re=0.1$. Simulations are performed for differing numbers of fibers, $M=50, 100, 200$ and 400. The individual fiber length is set to $L=0.1$, and the grid size is set to $h=0.01$. We use $Q=11$ marker in each fiber; thus, $\Delta l=h=0.01$.

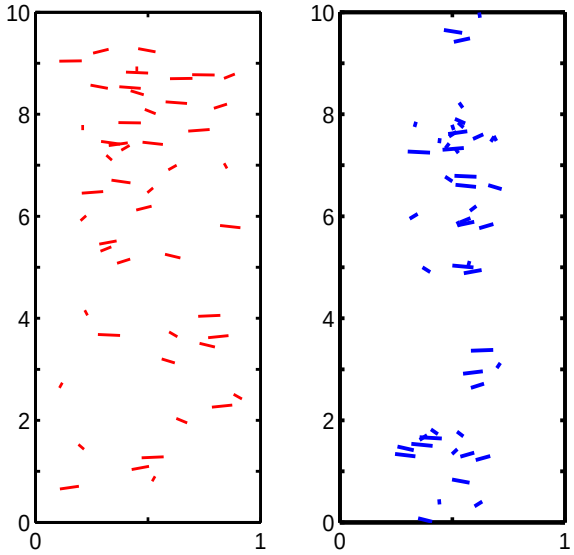

Figure 1: Plots of the suspension of 50 fibers at (a) $t=0$ and (b) $t=100$. The Reynolds number $Re=0.1$. Fibers are randomly distributed at $t=0$. At $t=100$, fibers have formed clusters and aggregated towards the center line $x=0.5$.

Fig. 1 shows the distribution of 50 fibers at $t=0$ and $t=100$. (We note that in all the figures showing fiber distribution in this paper, the vertically oriented fibers appear much shorter than horizontal ones due to the large $y:x$ aspect ratio. These fibers indeed have the same length.) The fibers are initially randomly distributed. At $t=100$, fibers have aggregated and formed fiber-rich areas (i.e., clusters). In particular, the fibers tend to aggregate along the vertical center line of the box, $x=0.5$. Figs. 2 and 3 show the distributions of 100 and 400 fibers, respectively, with the same initial setup. We observe

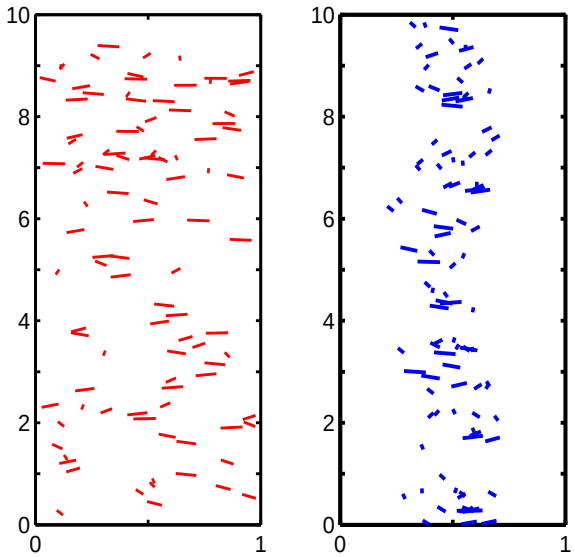

Figure 2: Plots of the suspension of 100 fibers at (a) $t=0$ and (b) $t=100$. The Reynolds number $Re=0.1$. Fibers are randomly distributed at $t=0$. At $t=100$, fibers show more pronounced aggregation than the $M=50$ case (see Fig. 1-(b)).

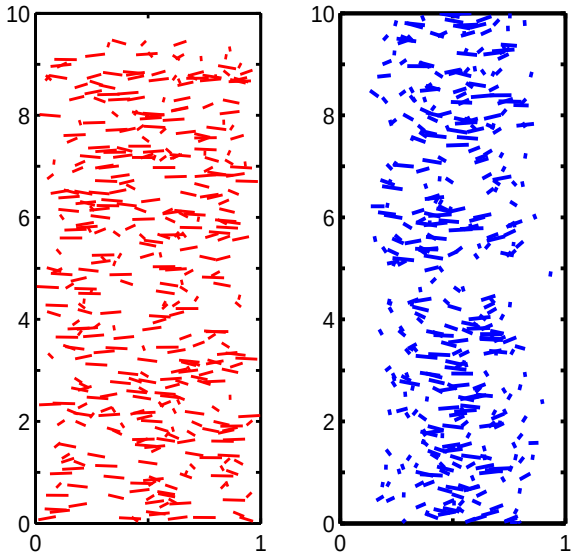

Figure 3: Plots of the suspension of 400 fibers at (a) $t=0$ and (b) $t=100$. The Reynolds number $Re=0.1$. Fibers are randomly distributed at $t=0$. At $t=100$, fiber clustering and centerline aggregation is significantly more pronounced than the cases with $M=50$ and $M=100$, shown in Figs. 1-(b) and 2-(b), respectively.

more pronounced aggregation behaviors as the number of fibers increases. These results suggest that at higher fiber density, the reduced average initial fiber separation increases inter-fiber hydrodynamic interactions, which tend to produce more pronounced clustering.

To quantify the degree of aggregation, we calculate the average distance between the fibers and the center line of the box, $x=0.5$, as a function of time. The average distance is defined by

$$\frac{1}{M}\sum_{m=1}^{M}|C_m-0.5|,$$

where M is the total number of fibers, and where C_m is the x-coordinate of the middle point of the mth fiber, i.e., $C_m=(X_{m,1}+X_{m,Q})/2$. The results are shown in Fig. 4 for $M=50,100,200$ and 400. The striking pattern of these curves is that the average distance for a fixed value of M generally decreases as time progresses. This result is consistent with the fiber clustering observed in experiments by Holm et al. [18].

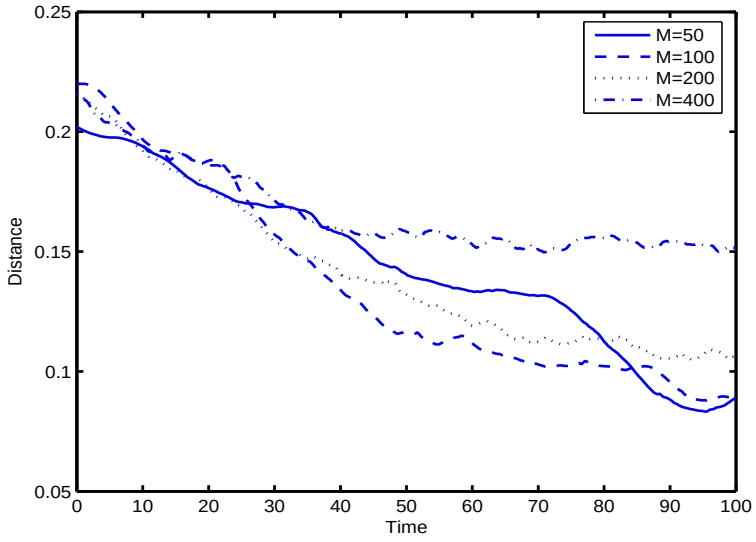

Figure 4: Average distance between the fiber midpoints and the center line of the box. Results are shown for $M=50,100,200$ and 400. The Reynolds number $Re=0.1$. A general decrease in the average distance is observed, indicating a fiber aggregation towards the center line.

Initially, in the above numerical simulations the fibers are randomly oriented; as time progresses, they tend to align themselves along the direction of gravity. In Fig. 5, we measure the mean orientation in the vertical direction for the suspending fibers. The mean orientation is calculated by averaging over all fibers the absolute value of the y-component of the unit direction vector. The calculation is performed for $M=50,100,200$ and 400, respectively. The results show that the mean orientation first increases, then approaches a steady state, with the value of that steady-state orientation slightly different

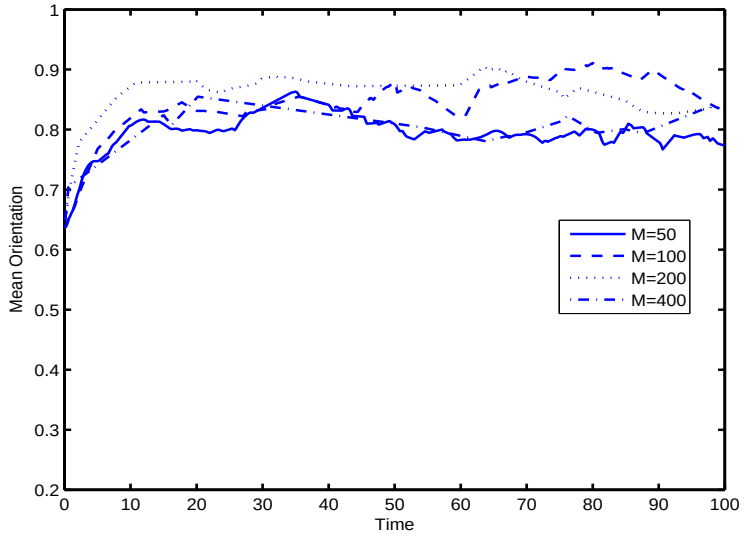

Figure 5: Mean orientation in the vertical direction for $M=50,100,200$ and 400. The Reynolds number $Re=0.1$. Given an initial randomly-distributed orientation, the fibers increasingly align along the vertical direction until a steady state is reached.

for different fiber density. The increase in the mean vertical orientation leads to increased sedimentation speed, which will be discussed in the next section. Similar observations were made in a numerical study by Tornberg and Gustavsson [31] for fiber suspensions in Stokes flows, and in experimental studies by Herzhaft et al. [16,17] under Stokes flow conditions. In [31], the authors performed numerical calculations for up to 100 fibers. Their measurements for the mean orientation with $M=100$ yield a steady-state value ≈ 0.7, which exhibits a reasonable agreement (within a 10% discrepancy) with our results. The slight difference can be attributed to the fact that our numerical simulations are performed with a small but nonzero Reynolds number. In [16] and [17], Herzhaft et al. experimentally studied the fiber orientation with a large set of fibers ($M=919$) by directly measuring the projected angles in radians. They found that the mean projected angle fluctuated approximately between 1.0 rad. and 1.2 rad., before reaching a steady-state value ≈ 1.1 rad. Note that $\sin(1.1\text{ rad.}) \approx 0.89$; thus, the experimental results by Herzhaft et al. are consistent with ours to a reasonable degree.

To further validate our numerical results, a convergence study in terms of the grid size, h, is provided for the average fiber-centerline distance and mean orientation. We use $h=0.04, 0.02, 0.01$ and 0.005, and perform the calculation from $t=0$ to $t=10$ with each choice of h for $M=50$ (representing low fiber density) and $M=400$ (representing high fiber density), respectively. Since no exact solutions are available for the current problem, we use the standard Richardson extrapolation to check the order of accuracy. Let $D(h)$ and $\Phi(h)$ denote the numerical solutions with the grid size h for the average

Table 1: Convergence study in h, the grid size, for 50 fibers. $D(h)$ and $\Phi(h)$ denote the numerical solutions for the average fiber-centerline distance and mean orientation, respectively. The values of $r(\cdot,h)$ indicate first-order convergence.

h	$D(h)$	$r(D,h)$	$\Phi(h)$	$r(\Phi,h)$
0.04	0.1961	1.22	0.8109	1.39
0.02	0.1954	1.58	0.8130	1.00
0.01	0.1951	–	0.8138	–
0.005	0.1950	–	0.8142	–

Table 2: Convergence study in h, the grid size, for 400 fibers. $D(h)$ and $\Phi(h)$ denote the numerical solutions for the average fiber-centerline distance and mean orientation, respectively. The values of $r(\cdot,h)$ again indicate first-order convergence.

h	$D(h)$	$r(D,h)$	$\Phi(h)$	$r(\Phi,h)$
0.04	0.1995	0.87	0.7814	1.08
0.02	0.1973	0.78	0.7831	1.23
0.01	0.1961	–	0.7839	–
0.005	0.1954	–	0.7842	–

fiber-centerline distance and mean orientation, respectively. We define

$$e(D,h)=|D(h)-D(h/2)|, \quad r(D,h)=\log_2[e(D,h)/e(D,h/2)],$$
$$e(\Phi,h)=|\Phi(h)-\Phi(h/2)|, \quad r(\Phi,h)=\log_2[e(\Phi,h)/e(\Phi,h/2)],$$

where $e(\cdot,h)$ gives the difference between two consecutive numerical runs with grid sizes h and $h/2$, and $r(\cdot,h)$ indicates the order of convergence with respect to h. The results are given in Table 1 for $M=50$ and Table 2 for $M=400$.

We observe typically first-order convergence in h from these tests. This is a generic feature of the immersed boundary method due to the use of discrete delta functions, which smooth out sharp interfaces to an "effective thickness" in the order of the grid size, h. We also note that the value of $D(h)$, which measures the fiber aggregation towards the center line, decreases in both tests when the grid is refined, showing higher degrees of fiber aggregation. This is due to the fact that smaller value of h leads to a decrease in the fiber effective thickness, thus results in a higher degree of aggregation among fibers.

All the results reported so far were obtained for initially randomly distributed fiber suspensions. In the next set of simulation, we consider a different initial configuration. Instead of a random distribution, we align these fibers together on the top of the box, as shown in Fig. 6-(a) for a suspension of 50 fibers. At $t=100$, the fibers have separated in the sense that fibers can be found at various vertical levels. Nonetheless, we observe more pronounced fiber clusters compared to the case of random initial distribution. Similar behaviors were observed for different fiber densities. These results suggest that in flows with small Reynolds numbers, the suspending fibers tend to form clusters, regardless of the initial configuration. Indeed, if initially the fibers are already aggregated to some ex-

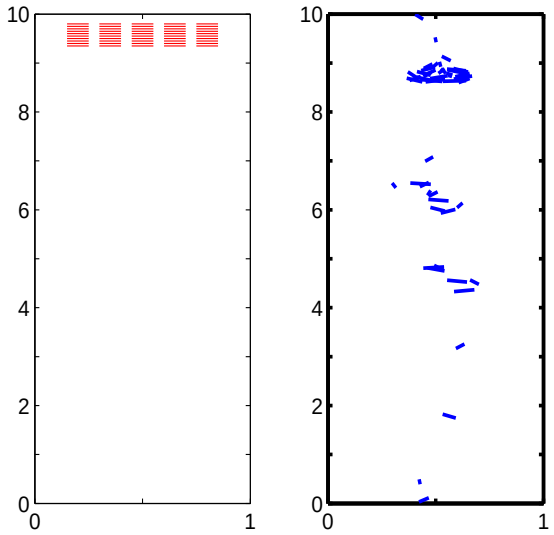

Figure 6: Plots of the suspension of 50 fibers at (a) $t=0$ and (b) $t=100$. The Reynolds number $Re=0.1$. Fibers are aligned on the top of the box at $t=0$. At $t=100$, fibers have formed clusters that are more pronounced than those in Fig. 1-(b).

tent, then the fiber-fluid interaction will strengthen that aggregation, thereby magnifying the heterogeneous structure.

3.2 Sedimentation velocity

In studies of particle suspensions, one is frequently interested in the average sedimentation velocity and its dependency on various factors. Thus, in the next set of simulations, we measure the average sedimentation velocity as time progresses for differing fiber densities. Results are shown in Fig. 7 for 50, 100, 200 and 400 fibers. The Reynolds number is 0.1 and the initial distribution is random in all these cases. As the number of fibers increases, the average sedimentation velocity also increases due to higher level of fiber aggregation as well as larger gravitational forces exerted on fibers which are subsequently transferred onto the fluid. Owing to the anisotropic nature of fibers, the dynamics of suspending fibers differs qualitatively from that of spheres in the strong dependency on particle orientation. In particular, individual fibers can have motion perpendicular to gravity. As noted previously, fibers increasingly align themselves along the gravitational (vertical) direction as time progresses. As their orientation becomes more vertical, the average vertical velocity increases correspondingly. As is clear from Fig. 7, for a fixed number of fibers, the average sedimentation velocity first grows with time, then reaches a steady state. This pattern is consistent with the measurement of the mean vertical orientation, shown in Fig. 5. Similar results were reported in [9, 16, 17, 31], for example, for three-dimensional Stokes flows. In all these studies, one observes that the average

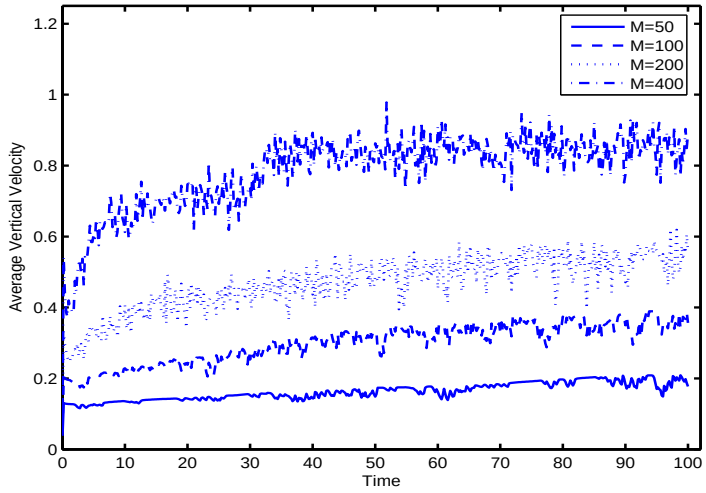

Figure 7: Average sedimentation velocity in the vertical direction for $M=50,100,200$ and 400. Results show that the sedimentation velocity (1) increases over time, approaching a steady state, and (2) increases with fiber density.

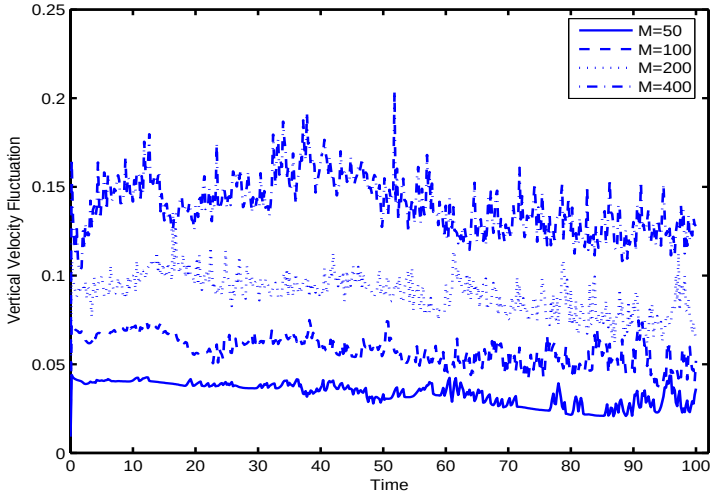

Figure 8: Vertical velocity fluctuation for $M=50,100,200$ and 400. Results show that vertical velocity fluctuation increases as fiber density increases.

sedimentation velocity increases over time and approaches a steady state. In [9, 31], it is also found that the average sedimentation velocity increases with higher fiber density. Although it is not possible to quantitatively compare our two-dimensional results of the sedimentation velocities with those published three-dimensional measurements, Fig. 7 does show clear trends which are consistent with those three-dimensional results.

Long-range hydrodynamic interactions among fibers cause the sedimentation veloc-

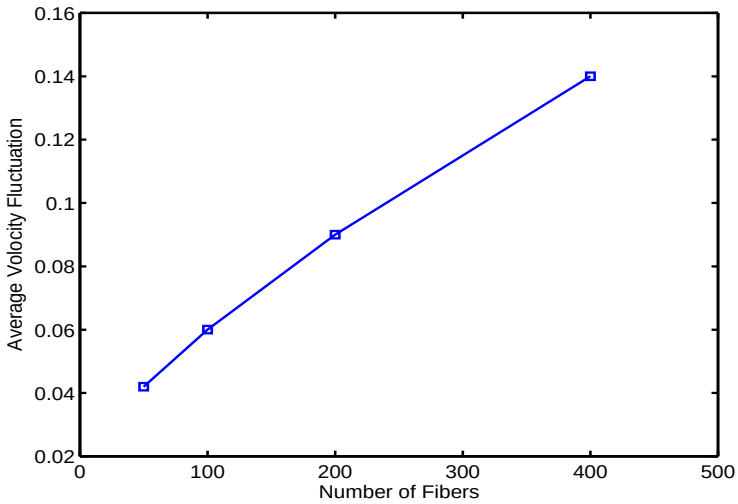

Figure 9: Time-averaged vertical velocity fluctuation as a function of the number of fibers. The results for $50, 100, 200$ and 400 fibers are marked with squares. The four data points lie on an approximate straight line, which suggests that average vertical velocity fluctuation increases linearly with fiber density.

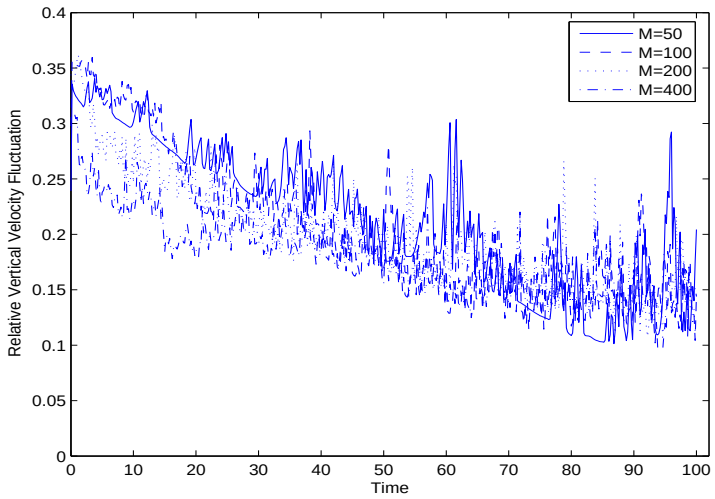

Figure 10: Relative velocity fluctuation for $M=50, 100, 200$ and 400. The measurements are not systematically distinguishable between the four sets of numerical experiments, a result that suggests that relative velocity fluctuation is independent of fiber density.

ity of individual fibers to fluctuate about the mean. The velocity fluctuation for the entire set of fibers is given by the standard deviation of the sedimentation velocities over all fibers. We compute the velocity fluctuation as time progresses for 50, 100, 200 and 400 fibers. The results, shown in Fig. 8, suggest that the velocity fluctuation increases with increasing fiber density owing to the higher degree of fiber-fiber interactions. To further understand the relation between fiber density and velocity fluctuation, we take the aver-

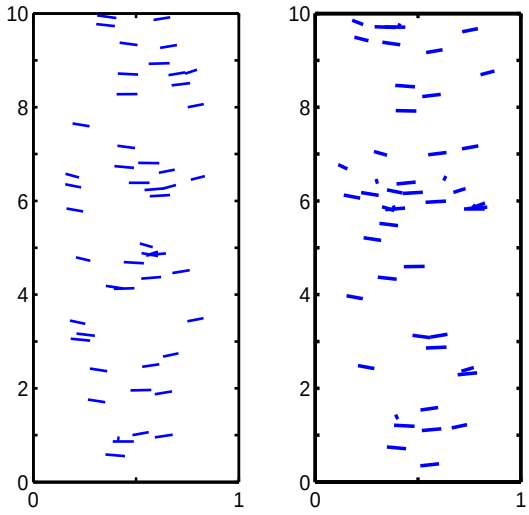

(a) (b)

Figure 11: The suspensions of 50 fibers at $t=100$ with the Reynolds number $Re=10$: (a) the fibers are randomly distributed at $t=0$ and (b) the fibers are aligned on the top of the box at $t=0$. The degree of aggregation at $t=100$ is significantly less than the $Re=0.1$ case.

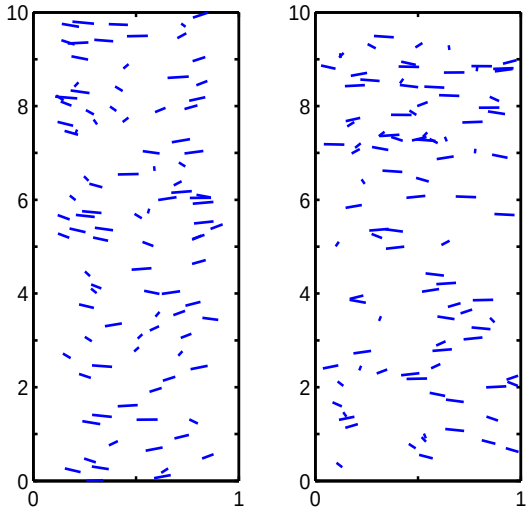

(a) (b)

Figure 12: The suspensions of 100 fibers at $t=100$ with the Reynolds number $Re=10$: (a) the fibers are randomly distributed at $t=0$ and (b) the fibers are aligned on the top of the box at $t=0$. The degree of aggregation at $t=100$ is significantly less than the $Re=0.1$ case.

age of the velocity fluctuation over the time interval $[0,100]$, and plot the average velocity fluctuation as a function of the number of fibers. The results approximate a straight line (see Fig. 9). This suggests that the average velocity fluctuation increases linearly with the number of fibers, which agrees with the results in [9]. Finally, if we consider the relative

velocity fluctuation, i.e., the ratio of the velocity fluctuation and the average sedimentation velocity, then we obtain almost the same profile for all the four choices of fiber numbers when $t \geq 20$, as shown in Fig. 10. This observation suggests that the long-term behavior of the relative velocity fluctuation is independent of the fiber density.

3.3 Effects of Reynolds numbers

Previous simulations are limited to the low Reynolds number regime ($Re = 0.1$). To assess the effects of the Reynolds number on the sedimentation process of fiber suspensions, we conduct additional simulations using a larger Reynolds number ($Re = 10$), which corresponds to a less viscous fluid. Two initial fiber configurations are considered: one in which the fibers are randomly distributed (see Fig. 1-(a)), and the other in which the fibers are top-aligned (see Fig. 6-(a)). Results are shown in Figs. 11 and 12 for 50 and 100 fibers, respectively. Unlike in the low Reynolds number case, we observe little evidence of aggregation at $t = 100$. In particular, in the case where the fibers are initially clustered at the top (Figs. 11-(b) and 12-(b)), the fibers become approximately randomly distributed throughout the domain at $t = 100$, showing evidence of dispersion.

To quantify the degree of aggregation (or the lack thereof) in the above simulations, we measure the average distance between the fibers and the center line of the box, and we measure the mean vertical orientation of the fibers. The results are shown in Figs. 13 and 14. In contrast to the corresponding results obtained for the low Reynolds number regimes (Figs. 4 and 5, respectively), both average fiber-centerline distance and the mean vertical orientation oscillate around their respective mean values, indicating that the fibers neither aggregate toward the center line of the box, nor do they align with the direction of gravity.

To better understand the different effects of high and low Reynolds numbers on the sedimentation dynamics, we perform a simple simulation of the sedimentation of only two fibers for $Re = 0.1$ and 10, and study the detailed hydrodynamic motion. By looking into the velocity field in the fluid, which is easy to visualize with two fibers, we gain essential information on the different behaviors of fiber-fluid interactions.

Fig. 15 depicts the sedimentation at $Re = 0.1$. Initially the two fibers are aligned near the top of the domain, as shown in Fig. 15-(a). At $t = 5$, they are already getting closer to each other (see Fig. 15-(b)). The velocity field in this case indicates that the two fibers will become even closer, since the upper fiber is more vertical, thus moving downwards at a higher speed, than the lower fiber. This is justified by the result at $t = 20$ (see Fig. 15-(c)), where the two fibers are now separated by only half of the initial distance. Moreover, at $t = 40$ (not shown), the distance between these two fibers is only one quarter of their initial distance. These results demonstrate that at a low Reynolds number, fibers approach each other due to the local velocity field.

In contrast, at $Re = 10$, the two sedimenting fibers behave differently; they depart from each other over time, as shown in Fig. 16. We start from the same initial profile as in Fig. 15-(a). At $t = 5$, the distance between the two fibers is already more than triple of

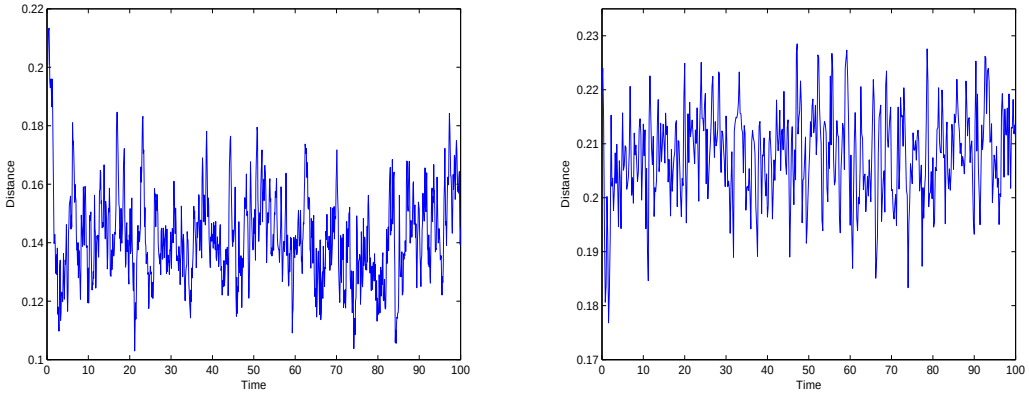

(a) (b)

Figure 13: Average distance between the fibers and the center line of the box with the Reynolds number $Re=10$: (a) 50 fibers and (b) 100 fibers. Results show no evidence of fiber aggregation towards the center line.

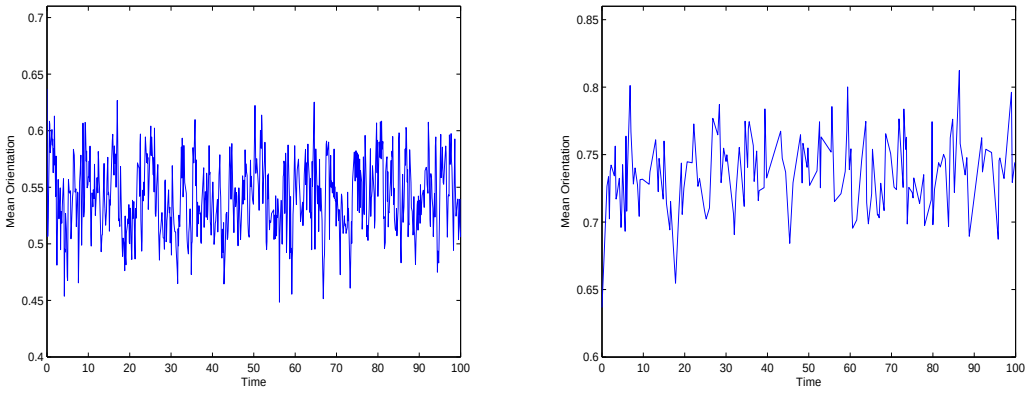

(a) (b)

Figure 14: Mean vertical orientation of the fibers with the Reynolds number $Re=10$: (a) 50 fibers and (b) 100 fibers. Results show no evidence of increasing vertical fiber alignment.

their initial distance (see Fig. 16-(b)). Based on the velocity field, one can observe that the fluid flow tends to pull the two fibers even further away from each other. Indeed, the result at $t=20$ (shown in 16-(c)) confirms this pattern.

3.4 Boundary effects

It is well known that domain boundary conditions have a significant impact on the dynamics of the enclosed fluid. In previous simulations, boundary conditions were set to be periodic along the y-direction, and homogeneous Dirichlet along the x-direction. In the next set of simulations, we investigate the effects of the horizontal boundary conditions

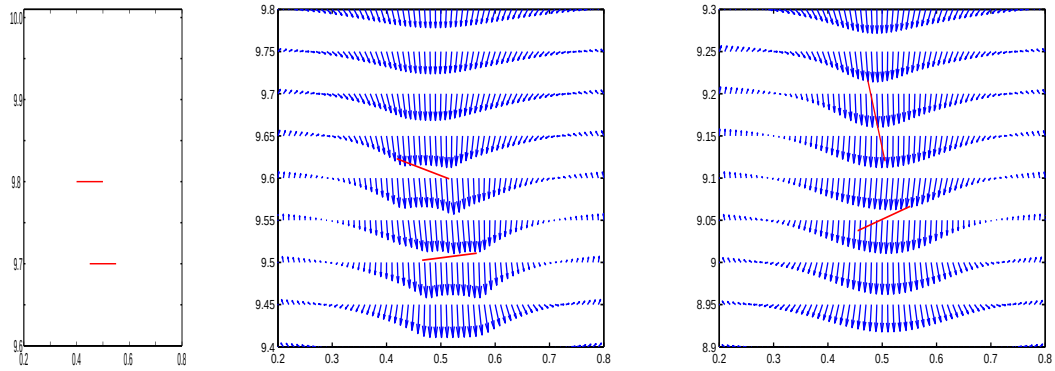

(a) (b) (c)

Figure 15: Sedimentation of two fibers at $Re=0.1$. The solid lines represent fibers, while the arrows represent the velocity field in the fluid: (a) $t=0$, (b) $t=5$ and (c) $t=20$. Results show that the two fibers are approaching each other over time.

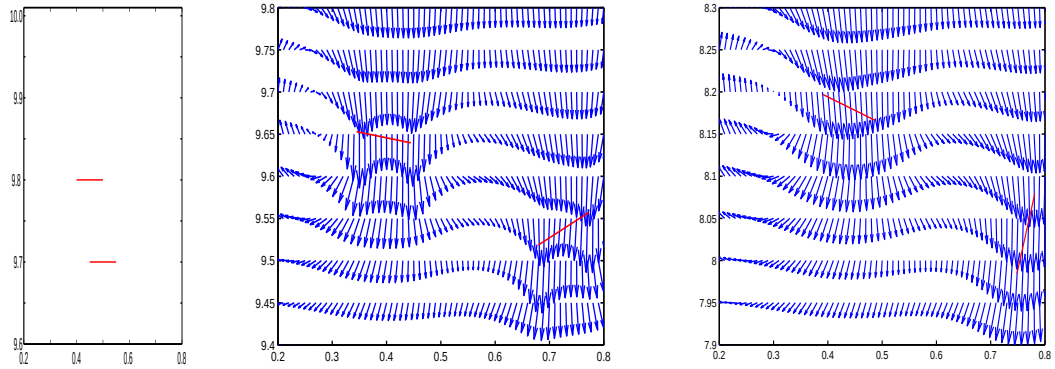

(a) (b) (c)

Figure 16: Sedimentation of two fibers at $Re=10$. The solid lines represent fibers, while the arrows represent the velocity field in the fluid: (a) $t=0$, (b) $t=5$ and (c) $t=20$. Results show that the two fibers are pulled away from each other over time.

on the fiber suspension. To that end, we conduct simulations assuming that the boundary conditions are biperiodic (in both x- and y-directions), and we perform the Fast Fourier Transform in both spatial directions. In Fig. 17, we show the distributions of 50 fibers with periodic horizontal boundaries at $t=100$, again for two choices of initial configurations: one with random distribution and the other with regular alignment. The Reynolds number is set to $Re=0.1$ in both cases. Compared with Figs. 1, 6 and 11, we see that the fibers with periodic boundaries in the x-direction do aggregate, but not as much as those with solid boundaries. The reason is that with periodic boundaries, fibers have more freedom to move in the direction perpendicular to gravity, thus they are less inclined to

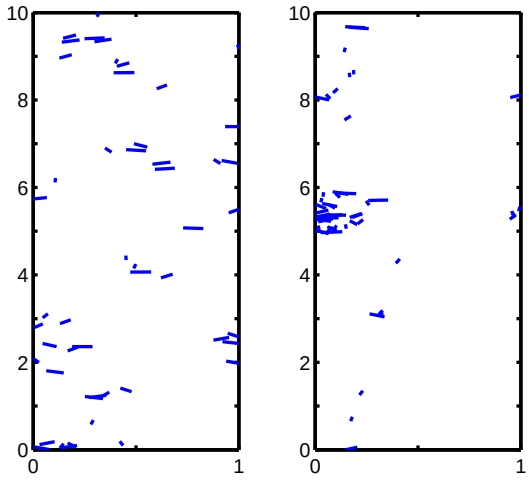

Figure 17: The suspensions of 50 fibers at $t=100$ with periodic boundary conditions in the x-direction: (a) the fibers are randomly distributed at $t=0$ and (b) the fibers are aligned on the top of the box at $t=0$. In both cases, the degree of aggregation is less than the corresponding case with solid boundaries in the x-direction.

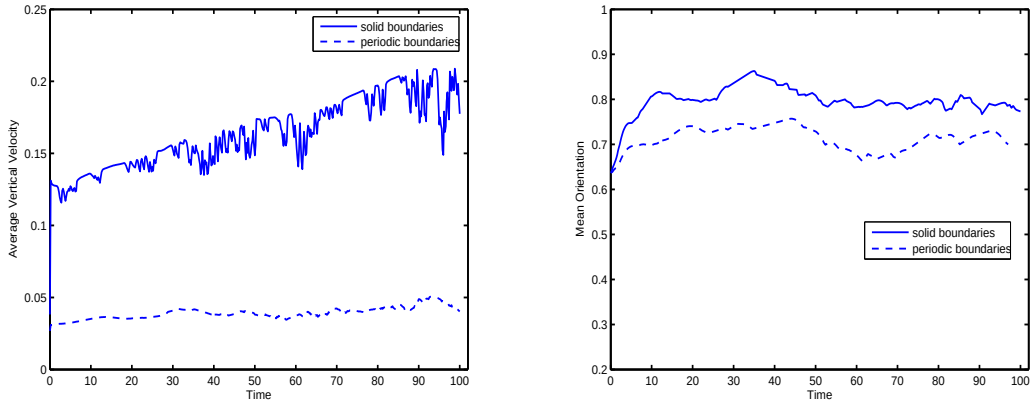

Figure 18: Comparison of (a) average sedimentation velocity and (b) mean vertical orientation between fiber suspension with solid boundaries and that with periodic boundaries. The number of fibers is 50 and they are randomly distributed initially.

cluster in a certain area. As a result of this reduced degree of clustering, fibers with periodic boundaries have a smaller average sedimentation velocity than those with solid boundaries. We also observe that the mean vertical orientation of fibers with periodic boundaries is smaller than that in the solid-wall case. These comparisons are presented in Fig. 18 with 50 fibers. Similar results were obtained when varying the number of fibers (not shown).

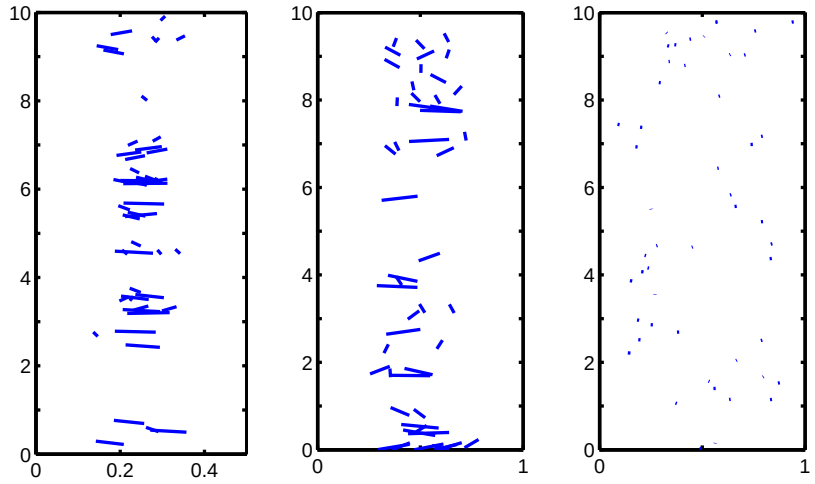

Figure 19: The suspensions of 50 fibers at $t=100$ with different domain size or fiber length: (a) the domain is $[0,0.5]\times[0,10]$ and the fiber length is 0.1, (b) the domain is $[0,1]\times[0,10]$ and the fiber length is 0.2, and (c) the domain is $[0,1]\times[0,10]$ and the fiber length is 0.01. When volume fraction is increased either by reducing the domain size (a) or increasing the fiber length (b), the clustering effect is enhanced; and vice versa (c).

3.5 Domain size and fiber length

In Sections 3.1 and 3.2 we investigated the effects of fiber density on the sedimentation process, and we varied fiber density by varying the number of fibers in a fixed domain size. However, increasing the number of fibers also has the effect of increasing the gravitational force exerted by the immersed fibers on the underlying fluid, the effect of which is unclear. Thus, in the next set of simulations, we fix the number of fibers (and thus the total gravitational force) and vary the fiber density by varying the domain size. We obtain results for a domain size that is half of the base-case, $[0,0.5]\times[0,10]$ and for 50 fibers; the fiber distribution at $t=100$ is shown in Fig. 19-(a). With the domain size reduced to half, the fiber density is doubled, with the total gravitational force unchanged. Compared to the base-case results (Fig. 1), a larger degree of aggregation is observed, consistent with our previous conclusion that a higher fiber density increases fiber clustering.

For a fixed domain size and a fixed fiber density, the volume fraction taken up by the fibers may be varied by varying the individual fiber length. To assess the impact of fiber length on the dynamical behavior, we conduct simulation for fiber length $L=0.2$ and 0.01. (The base-case fiber length is $L=0.1$.) For the longer-fiber case ($L=0.2$), the volume fraction of fibers is double that of base case. The higher volume fraction increases the hydrodynamic interactions among the fibers, and fiber aggregation becomes more pronounced (see Fig. 19-(b)). In contrast, with the fiber length reduced to 1/10 of base-case length, the dynamics of the fiber suspension approach that of spherical particles. In particular, compared to base case, the movement of fibers along the horizontal direction is much reduced, and the fibers show little tendency to aggregate. Indeed, at $t=100$,

these almost-spherical fibers are found throughout the entire box. They do not aggregate towards the center line of the box, and no cluster have formed (see Fig. 19-(c)).

4 Discussion

In this study, the sedimentation of fiber suspensions is formulated as an immersed boundary problem. The salient feature of the immersed boundary approach is the ability to explore a wide range of parameters, including fiber density, initial configuration, Reynolds number, domain boundary condition, domain size, and fiber length, all of which contribute to the complex dynamics in the sedimentation process. The numerical algorithm is capable of computing a large number of suspending fibers, and allows long-time simulations so that steady-state sedimentation behaviors can be observed. Our numerical results in low Reynolds number regime agree with the experimental and numerical measurements of fiber suspensions in Stokes flows, i.e., the limit of zero Reynolds number. In particular, the behaviors of fiber clustering are confirmed in our numerical study, and it is observed that higher fiber densities generate higher degree aggregations. In contrast, we have found that in the high Reynolds number regime, the suspending fibers exhibit dispersion instead of aggregation. We have also carefully measured the average sedimentation properties to further understand the dynamics under differing conditions.

Using a method based on non-local slender body approximation, Tornberg and co-workers simulated sedimentation of rigid and flexible fiber suspensions in Stokes flows [31,32]. The settling and clustering dynamics revealed in their studies are consistent with our results for low Reynolds numbers. The models by Tornberg and co-workers are in three spatial dimensions, and thus are, in some sense, more realistic than the present model. One difference between fiber suspensions in two- and three-dimensional domains is that the latter enjoy more freedom in their movements: in a two-dimensional model, fibers that overlap in the horizontal dimension cannot overtake each other. Our model can be generalized to three dimensions, at the expense of a substantial increase in computational cost. Despite its limitations, our model allows simulations with arbitrary Reynolds numbers and domain shapes — flexibility that may be difficult to achieve in a Stokes flow model such as [31,32].

In addition to higher spatial dimensions, the current model can be extended in a number of other interesting directions. One example is the simulation of self-propelled elongated particles. Instead of being pulled by gravity, the fibers can move in a general direction with small fluctuations, as in bacteria swimming down a concentration gradient. Another example is the simulation of charged particles, which interact by attracting or repelling each other.

References

[1] M.-C. Anselmet, Contribution à l'étude DPs systéme fluid-particules: suspensions de cylindres, lits, fluidisés, Thése, Université de Provence, 1989.

[2] K.M. Arthurs, L.C. Moore, C.S. Peskin, E.B. Pitman and H.E. Layton, Modeling arteriolar flow and mass transport using the immersed boundary method, J. Comput. Phys. 147 (1998) 402-440.
[3] G.K. Batchelor, Sedimentation in a dilute dispersion of spheres, J. Fluid Mech. 123 (1972) 245-268.
[4] J.B. Bell, P. Colly and H.M. Gall, A second order projection method for the incompressible Navier-Stokes equations, J. Comput. Phys. 85 (1989) 257-283.
[5] R.P. Beyer, A computational model of the cochlea using the immersed boundary methods, J. Comp. Phys. 98 (1992) 145-162.
[6] R.P. Beyer and R.J. LeVeque, Analysis of a one-dimensional model for the immersed boundary method, SIAM J. Numer. Anal. 29 (1992) 332-364.
[7] J. Blake, Fluid mechanics of cilliary propulsion, Computational Modeling in Biological Fluid Dynamics (editor: L.J. Fauci and S. Gueron), Springer-Verlag: NY, 1999.
[8] D.L. Brown, R. Cortez and M.L. Minion, Accurate projection methods for the incompressible Navier-Stokes equations, J. Comput. Phys. 168 (2001) 464-499.
[9] J.E. Butler and E.S.G. Shaqfeh, Dynamic simulation of the inhomogeneous sedimentation of rigid fibers, J. Fluid Mech. 468 (2002) 205-237.
[10] R. Cortez and M. Minion, The blob projection method for immersed boundary problems, J. Comput. Phys. 161 (2000) 428-453.
[11] R.H. Davis and A. Acrivos, Sedimentation of noncolloidal particles at low Reynolds number, Ann. Rev. Fluid Mech. 17 (1985) 91-118.
[12] R. Dillon, L. Fauci and D. Gaver III, A microscale model of bacterial swimming, chemotaxis, and substrate transport, J. Theor. Biol. 177 (1995) 325-340.
[13] X. Fan, N. Phan-Thien and R. Zheng, A direct simulation of fibre suspensions, J. Non-Newtonian Fluid Mech. 74 (1998) 113-135.
[14] L. Fauci and A. McDonald, Sperm mobility in the presence of boundaries, Bull. Math. Biol. 57 (1995) 679-699.
[15] D. Goldstein, R. Handler and L. Sirovich, Modeling a no-slip flow boundary with an external force field, J. Comput. Phys. 105 (1993) 354-366.
[16] B. Herzhaft and É. Guazzelli, Experimental study of the sedimentation of dilute and semi-dilute suspensions of fibers, J. Fluid Mech. 384 (1999) 133-158.
[17] B. Herzhaft, É. Guazzelli, M.B. Mackaplow and E.S.G. Shaqfeh, Experimental invsetigation of the sedimentation of a dilute fiber suspension, Phys. Rev. Lett. 77 (1996) 290-293.
[18] R. Holm, S. Storey, M. Martinez and D. Soderberg, Visualization of streaming-like structures during settling of dilute and semi-dilute rigid fiber suspension, Phys. Fluid (accepted).
[19] M.M. Hopkins and L.J. Fauci, A computational model of the collective fluid dynamics of motile micro-organisms, J. Fluid Mech. 455 (2002) 149-174.
[20] E. Kuusela, K. Hofler and S. Schwarzer, Computation of particle settling speed and orientation distribution in suspensions of prolate spheroids, J. Eng. Math. 41 (2001) 221-235.
[21] M.C. Lai and C.S. Peskin, An immersed boundary method with formal second-order accuracy and reduced numerical viscosity, J. Comput. Phys. 160 (2000) 705-719.
[22] R. J. LeVeque and Z. Li, The immersed interface method for elliptic equations with discontinuous coefficients and singular sources, SIAM J. Numer. Anal. 31 (1994) 1019-1044.
[23] R. Mittal and G. Iaccarino, Immersed boundary methods, Ann. Rev. Fluid Mech., 37 (2005) 239-261.
[24] P.J. Mucha, S.Y. Tee, D.A. Weitz, B.I. Shraiman and M.P. Brenner, A model for velocity fluctuations in sedimentation, J. Fluid Mech. 501 (2004) 71-104.

[25] C.S. Peskin, Numerical analysis of blood flow in the heart, J. Comput. Phys. 25 (1977) 220-252.
[26] C.S. Peskin, The immersed boundary method, Acta Numer. 11 (2002) 479-517.
[27] J.F. Richardson and W.N. Zaki, Sedimentation and fluidization: Part I, Trans. Inst. Chem. Engrs. 32 (1954) 35-53.
[28] J.M. Stockie and S.I. Green, Simulating the motion of flexible pulp fibres using the immersed boundary method, J. Comput. Phys. 147 (1998) 147-165.
[29] J.M. Stockie and B.R. Wetton, Analysis of stiffness in the immersed boundary method and implications for time-stepping schemes, J. Comput. Phys., 154 (2007) 41-64.
[30] K. Taira and T. Colonius, The immersed boundary method: A projection approach, J. Comput. Phys., 225 (2007) 2118-2137.
[31] A.K. Tornberg and K. Gustavsson, A numerical method for simulations of rigid fiber suspensions, J. Comput. Phys. 215 (2006) 172-196.
[32] A.K. Tornberg and M.J. Shelley, Simulating the dynamics and interactions of flexible fibers in Stokes flow, J. Comput. Phys. 196 (2004) 8-40.
[33] M.A. Turney, M.K. Cheung, M.J. McCarthy and R.L. Powell, Hindered settling of rod-like particles measured with magnetic resonance imaging, AIChE J. 41 (1995) 251-257.